

Four-wave mixing in a Bloch two-level system with incoherent laser light having a Lorentzian spectral density: Analytic solution and a diagrammatic approach

Darin J. Ulness* and A. C. Albrecht†

Department of Chemistry, Cornell University, Ithaca, New York 14853-1301

(Received 21 August 1995)

Degenerate four-wave mixing using broadband, non-transform-limited (incoherent) laser light having a Lorentzian spectral density is treated analytically for a Bloch two-level system. We consider the configuration in which an incoherent beam from a Lorentzian source is split into two beams having distinct k vectors, \mathbf{k} and \mathbf{k}' . The twin beam along \mathbf{k}' has been subjected to a controllable delay, τ , relative to \mathbf{k} . These twin beams, focused into the sample of interest, generate new fourth fields, the signal at $\mathbf{k}_s = 2\mathbf{k} - \mathbf{k}'$ being examined here as a function of τ . A set of factorized time correlation (FTC) diagrams is introduced to organize the calculation and to yield both analytic expressions as well as physical insight. Not only is the signal not symmetric in τ but the signal can peak at $\tau \neq 0$ even in the absence of inhomogeneous broadening. Finally, the physical insights and the use of the FTC diagrams are extended to rationalize several other incoherent light spectroscopies.

PACS number(s): 42.50.Md, 42.62.Fi, 42.65.Re

I. INTRODUCTION

In the early 1980s it was discovered how non-transform-limited, broadband (incoherent or noisy) light could be used in nonlinear-optical spectroscopies to probe subpicosecond material dynamics [1,2]. Since its first application in two-beam photon-echo-like experiments, noisy light has been used in many different time-domain nonlinear-optical spectroscopies such as in three-beam degenerate and nondegenerate four-wave mixing (4WM) [3], coherent anti-Stokes Raman scattering (CARS) and coherent Stokes Raman scattering (CSRS) [4–6], and the optical Kerr effect [7]. In the frequency domain, novel ultrasharp spectral “poles” have been discovered [8,9]. Review articles have appeared [9,10]. In this paper we seek analytic solutions to 4WM in a Bloch two-level system with full attention to the time correlators that arise in the problem.

The principal idea in the use of noisy light for ultrashort timing is that, as opposed to traditional femtosecond work, it is the coherence time τ_c of the light, not the temporal profile of its pulses, that determines the time resolution. In principle, the noisy beam may be cw, although in practice it is very often on the order of pulses generated by a neodymium-doped yttrium aluminum garnet (Nd:YAG) laser, i.e., nanoseconds. The coherence time of the light produced by standard dye lasers operating in broadband mode is typically on the scale of hundreds of femtoseconds but may, with wider spectral densities, be tens of femtoseconds. The incoherent source enters the optics of a Michelson interferometer to generate identical twin beams (assuming perfect optics) one of which is delayed by τ over the other by use of a controllable spatial delay in one of the arms of the interferometer. The twin beams are configured to enter the sample along unique k vectors, one along \mathbf{k} and its twin (τ shifted) along \mathbf{k}' . The fourth waves appear along several new k vectors, a

particular one, such as $\mathbf{k}_s = 2\mathbf{k} - \mathbf{k}'$, is spatially isolated, possibly spectrally filtered, and quadrature detected (intensity). The fourth-wave intensity plotted against τ generates a signal called an interferogram. Clearly, the signal along $\mathbf{k}_{s'} = 2\mathbf{k}' - \mathbf{k}$ generates an interferogram which is the complement (mirror image) of that of $\mathbf{k}_s = 2\mathbf{k} - \mathbf{k}'$.

Two important considerations arise in the theoretical treatment of the signal produced in noisy beam experiments. First, all possible time orderings of field interventions on the sample must be included. That is to say, the field from one or the other of the twin noisy beams may act first and/or second, etc. As far as femtosecond or picosecond dynamics are concerned the light fields that appear in the form of nanosecond or longer pulses are effectively continuously present. By contrast, in most femtosecond treatments the time ordering of the fields is considered to be under experimental control. Second, one must properly treat the noise and the correlation between the twin beams. Since the 4WM signal is quadrature detected, explicit use of the so-called *bichromophoric model* [4] appears and averaging over the stochastic properties of the fields occurs at the signal level where fourth fields from two independent chromophores are involved. As in normal 4WM the density operator $\hat{\rho}$ is solved perturbatively to third order to give the third-order electrical polarization (or its Fourier transform) which is taken to quadrature. The stochastic averaging over the noisy light fields is now superimposed and appears as a six-point time correlator.

The present study carries this procedure to an analytic conclusion for degenerate 4WM (D4WM) in a two-level system having no permanent dipole using incoherent light of Lorentzian spectral density. As shown in Fig. 1, we consider the spatially resolved signal at $\mathbf{k}_s = 2\mathbf{k} - \mathbf{k}'$ where \mathbf{k} and \mathbf{k}' are the two distinct k vectors of the twin beams. This type of experiment is designated as *two-beam* $I^{(3)}$ D4WM. In general, $I^{(n)}$ indicates n perturbative actions of the noisy (or incoherent) field (in 4WM using only noisy fields, n is necessarily 3). Exploring such a simple model is of interest because, at the 4WM level where each of the three field interventions carries a broadband (here Lorentzian) spectral profile, a generally extremely difficult calculation becomes at least amenable in the simple Bloch model. Then the analytic

*Electronic address: DU11@CORNELL.EDU

†Electronic address: ACA7@CORNELL.EDU

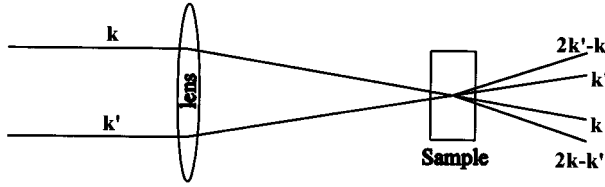


FIG. 1. Beam configuration for *two-beam* $I^{(3)}$ D4WM. We consider the signal $\mathbf{k}_s = 2\mathbf{k} - \mathbf{k}'$.

result provides a basis for a more general understanding of the $I^{(3)}$ D4WM interferograms.

In dealing with the time correlators that arise in the $I^{(3)}$ D4WM problem a diagrammatic technique involving factorized time correlators (FTC's) is introduced. It is found how simple rules lead directly from the FTC diagrams to an important limiting form of the exact analytic solution. Just as important, the FTC diagrams offer qualitative "physical" insight of wide use that provides a tool for understanding asymmetric interferograms, peaking of the signal at $\tau \neq 0$, limiting peak-to-background ratios (the signal contrast), and finally useful qualitative and sometimes quantitative relationships among several incoherent light spectroscopies.

II. EVOLUTION OF THE DENSITY MATRIX

The semiclassical approach with density-operator formalism in which the classical field acts as a perturbation is common in nonlinear optics [12]. The integral form of the n th-order density-operator matrix elements in the two-level basis set is a starting point with Appendix A of the original paper of Morita and Yajima [1] a useful reference.

We seek the $I^{(3)}$ D4WM signal (as a function of τ) along $\mathbf{k}_s = 2\mathbf{k} - \mathbf{k}'$ which is a third-order process. In general there are 48 terms in the third-order expansion of the density-operator matrix elements [13] (eight Liouville paths with $3!$ field permutations each). Here the number of terms is reduced to 24 due to the indistinguishability of two of the three field interventions. Thus at the mod square level 24×24 terms appear (before any stochastic averaging). The calculation rapidly becomes daunting. To facilitate analytic calculations and to capture the essence of the signal we contend throughout that the signal is dominated only by those terms which enjoy full (in this case triple) resonance within the two-level system. It greatly aids in the organization of the calculation to express the matrix elements of the density operator diagrammatically. There are several such techniques [10]. Here the diagrammatic technique of Lee and Albrecht [11] is convenient for it immediately exposes any and all resonances. An upper-case D in the word Diagram is used when referring to diagrams representing density matrix elements, to avoid confusion with the FTC diagrams to appear later when performing the averaging over the noise in the light. The triple-resonance requirement reduces the 24 terms to only 2. The corresponding two Diagrams (or terms), referred to as D_1 and D_2 (their respective conjugates as D_1^* and D_2^*), are shown in Fig. 2 (the remaining 22 Diagrams can be readily constructed following simple rules [11]). In constructing all the Diagrams there actually are altogether four triply resonant Diagrams. In addition to D_1 and D_2

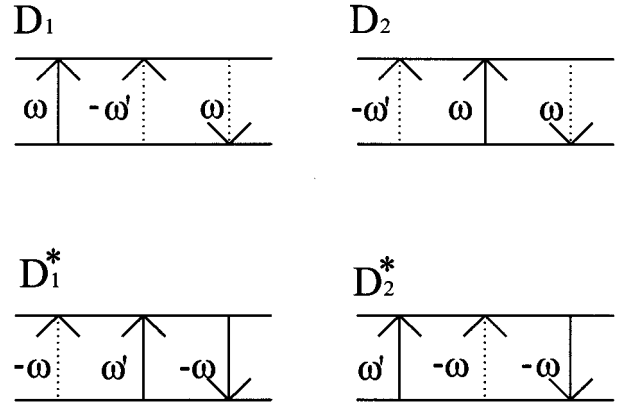


FIG. 2. The two fully resonant diagrams for triply resonant *two-beam* $I^{(3)}$ D4WM and their complex conjugates. Solid arrows represent ket-side evolution of the density matrix and dashed lines represent bra-side evolution. For more details see Lee and Albrecht [11].

there are two Diagrams which populate the ground state after the second intervention. Their contribution to the third-order polarization is analytically equivalent to that of D_1 and of D_2 under the condition of conservation of the trace of the density operator [4,19].

A. The integral equations up to third order

The main focus here is entirely in the time domain. For convenience the tensor notation is suspended and the treatment is reduced to a scalar one. The k vectors \mathbf{k} and \mathbf{k}' are distinct in order to spatially resolve the signal (through phase matching). However, the angle between them is assumed small so that their general direction of propagation can be taken to be along the z axis, allowing the field to be expressed as $\mathbf{E}(\mathbf{r}t) \Rightarrow \mathbf{E}(z,t)$. Appropriate orientational averaging of the elements of the dipole moment vector operator projected onto the (assumed) identically polarized twin beams leaves an effective scalar transition dipole moment μ and a scalar field $E(z,t)$.

The density matrix elements for each of the two triply resonant Diagrams for the two-level (m upper, g lower) system are derived. At n th order the integral equation for the m gth density matrix element is

$$\rho_{mg}^{(n)}(t) = \frac{i\mu}{\hbar} \int_{-\infty}^t dt_1 E(z,t_1) \rho_D^{(n-1)} e^{(-i\omega_{mg} - \gamma_{mg})(t-t_1)}, \quad (1)$$

with $\rho_{mg} = \rho_{gm}^*$ where

$$\rho_D^{(n-1)}(t) = \frac{i\mu}{\hbar} \int_{-\infty}^t dt_1 E(z,t_1) (\rho_{mg}^{(n-2)} - \rho_{gm}^{(n-2)}) e^{-\gamma_{mm}(t-t_1)}, \quad (2)$$

and $\rho_D \equiv \rho_{gg} - \rho_{mm}$, $\mu \equiv \mu_{mg} = \mu_{gm}$, the dipole moment matrix elements, $\gamma_{mg} \equiv 1/T_2$ and $\gamma_{mm} \equiv 1/T_1$, and ω_{mg} is the Bohr frequency of the two-level system. Building up to third

order from a cold thermal ensemble prior to t_1 [$\rho_D^{(0)}(t_1) = \rho_0$, $\rho_{mg}^{(0)}(t_1) = 0$] we have $\rho_D^{(1)}(t_2) = 0$,

$$\rho_{mg}^{(1)}(t_2) = \frac{i\mu}{\hbar} \int_{-\infty}^{t_2} dt_1 E(z, t_1) \rho_0 e^{(-i\omega_{mg} - \gamma_{mg})(t_2 - t_1)}, \quad (3)$$

$$\begin{aligned} \rho_D^{(2)}(t_3) &= \frac{2i\mu}{\hbar} \int_{-\infty}^{t_3} dt_2 E(z, t_2) \\ &\times \left(\frac{i\mu}{\hbar} \int_{-\infty}^{t_2} dt_1 E(z, t_1) \rho_0 e^{(-i\omega_{mg} - \gamma_{mg})(t_2 - t_1)} \right. \\ &\left. + \frac{i\mu}{\hbar} \int_{-\infty}^{t_2} dt_1 E(z, t_1) \rho_0 e^{(+i\omega_{mg} - \gamma_{mg})(t_2 - t_1)} \right) \\ &\times e^{-\gamma_{mm}(t_3 - t_2)}, \end{aligned} \quad (4)$$

and

$$\begin{aligned} \rho_{mg}^{(3)}(t) &= \frac{i\mu}{\hbar} \int_{-\infty}^t dt_3 E(z, t_3) \left[\frac{2i\mu}{\hbar} \int_{-\infty}^{t_3} dt_2 E(z, t_2) \right. \\ &\times \left(\frac{i\mu}{\hbar} \int_{-\infty}^{t_2} dt_1 E(z, t_1) \rho_0 e^{(-i\omega_{mg} - \gamma_{mg})(t_2 - t_1)} \right. \\ &\left. + \frac{i\mu}{\hbar} \int_{-\infty}^{t_2} dt_1 E(z, t_1) \rho_0 e^{(+i\omega_{mg} - \gamma_{mg})(t_2 - t_1)} \right) \\ &\left. \times e^{-\gamma_{mm}(t_3 - t_2)} \right] e^{(-i\omega - \gamma_{mg})(t - t_3)}. \end{aligned} \quad (5)$$

Simplifying Eq. (5) we have finally

$$\begin{aligned} \rho_{mg}^{(3)}(t) &= -2i\rho_0 \left(\frac{\mu}{\hbar} \right)^3 \int_{-\infty}^t dt_3 \int_{-\infty}^{t_3} dt_2 \int_{-\infty}^{t_2} dt_1 E(z, t_3) \\ &\times E(z, t_2) E(z, t_1) e^{-\gamma_{mm}(t_3 - t_2)} e^{-\gamma_{mg}(t - t_3 + t_2 - t_1)} \\ &\times [e^{-i\omega_{mg}(t - t_3 + t_2 - t_1)} + e^{-i\omega_{mg}(t - t_3 - t_2 + t_1)}]. \end{aligned} \quad (6)$$

B. The bichromophoric model

It is general for all 4WM that in order to obtain a non-trivial phase-matching condition (in other words a macroscopically resolvable signal k vector) one needs fourth waves derived from at least two spatially separated chromophores [4]. Furthermore, the signal field is normally quadrature detected. This means that the signal is derived from the modulus square of the sum of chromophore-derived fourth fields at the detector. The cross terms fully dominate such a signal so that the quadrature signal must be drawn from fourth fields derived from two separate chromophores (summed over all pairs). This is known as the *bichromophoric model* and is particularly important to the understanding of the incoherent light spectroscopies. A more complete and analytic discussion of the bichromophoric model is found in [4]. In any case, if Eq. (6) holds for one chromophore (t time line) we have for a second chromophore (s time line)

$$\rho_{mg}^{(3)}(s) = \text{Eq. (6) with } t_1 \rightarrow s_1, t_2 \rightarrow s_2, t_3 \rightarrow s_3, t \rightarrow s. \quad (7)$$

C. The noisy field

The total field E appearing in Eqs. (6) and (7) is now dissected for its components which produce the $I^{(3)}$ D4WM signal of interest. For easy reference it is useful to give distinct labels F and F' to the twin fields. Here F is the field associated with the beam having its k vector along \mathbf{k} . F is also the field which acts twice in the formation of the $I^{(3)}$ D4WM signal. Likewise, F' is the field associated with the beam having k vector \mathbf{k}' . F' acts only once in the present $I^{(3)}$ D4WM case and it also carries the time-delay parameter τ .

The general expression for the field at position \mathbf{r} at time t is the sum of all fields present. Here $E(z, t) = E_{\mathbf{k}}(z, t) + E_{\mathbf{k}'}(z, t)$ (the total field due to the simultaneous presence of noisy fields F and F'). The electric field of F is given by

$$E_{\mathbf{k}}(z, t) = \frac{E_0}{2} p(t) e^{-i\omega t + ikz} + \frac{E_0}{2} p^*(t) e^{i\omega t - ikz}, \quad (8)$$

that of τ -delayed F' is

$$\begin{aligned} E_{\mathbf{k}'}(z, t) &= \frac{E_0}{2} p(t - \tau) e^{-i\omega(t - \tau) + ik'z} \\ &+ \frac{E_0}{2} p^*(t - \tau) e^{i\omega(t - \tau) - ik'z}, \end{aligned} \quad (9)$$

where $p(t)$ is a complex stochastic function carrying the noise information, ω is the carrier frequency, and E_0 is a constant amplitude (shared by F and F'). With these definitions $\tau > 0$ signifies that field F' lags behind F . The particular fourth wave along $\mathbf{k}_s = 2\mathbf{k} - \mathbf{k}'$ is generated by only a small subset of the ($4^3 = 64$) field terms in Eq. (6) [with Eqs. (8) and (9)]. Thus many of the terms resulting from the product of the three total fields acting at t_3 , t_2 , and t_1 (also s_3 , s_2 , and s_1) are inactive in producing the signal of interest and these may be eliminated from further consideration. In fact, the necessary field products can be taken directly from the Diagrams in Fig. 2. The three-field product associated with D_1 is

$$\begin{aligned} [E_{\mathbf{k}}(z, t_3) E_{\mathbf{k}'}(z, t_2) E_{\mathbf{k}}(z, t_1)]_{D_1} \\ \rightarrow \frac{E_0^3}{8} p(t_3) p^*(t_2 - \tau) p(t_1) e^{-i\omega(t_3 - t_2 + t_1 + \tau) + ik_s z}, \end{aligned} \quad (10)$$

and that for D_2 is

$$\begin{aligned} [E_{\mathbf{k}'}(z, t_3) E_{\mathbf{k}}(z, t_2) E_{\mathbf{k}}(z, t_1)]_{D_2} \\ \rightarrow \frac{E_0^3}{8} p(t_3) p(t_2) p^*(t_1 - \tau) e^{-i\omega(-t_3 - t_2 + t_1 + \tau) + ik_s z}. \end{aligned} \quad (11)$$

Likewise, the products of fields essential for D_1^* and D_2^* along the s line are, respectively,

$$\begin{aligned}
& [E_{\mathbf{k}'}(z, s_3)E_{\mathbf{k}'}(z, s_2)E_{\mathbf{k}}(z, s_1)]_{D_1^*} \\
& \rightarrow \frac{E_0^3}{8} p^*(s_3)p(s_2 - \tau)p^*(s_1) \\
& \quad \times e^{i\omega(s_3 - s_2 + s_1 + \tau) - ik_s z}, \tag{12}
\end{aligned}$$

and

$$\begin{aligned}
& [E_{\mathbf{k}'}(z, s_3)E_{\mathbf{k}}(z, s_2)E_{\mathbf{k}}(z, s_1)]_{D_2^*} \\
& \rightarrow \frac{E_0^3}{8} p^*(s_3)p^*(s_2)p(s_1 - \tau) \\
& \quad \times e^{i\omega(-s_3 - s_2 + s_1 + \tau) - ik_s z}. \tag{13}
\end{aligned}$$

Now, by careful inspection of Eqs. (6) and (7) the triply resonant terms (i.e., the integral expressions for Diagrams D_1 and D_2 and their conjugates) may be exposed. One matches the coefficients of ω_{mg} in Eqs. (6) and (7) (and their conjugates) with those of ω in Eqs. (10)–(13). More formal treatment confirms this procedure.

Suppressing all spatial factors, considering only the temporal aspects, we arrive at the integral expressions for the density matrix elements from the two triply resonant Diagrams and their conjugates. Using D_1 , D_2 , D_1^* , and D_2^* now to designate the matrix elements themselves, we have for the vector $\mathbf{k}_s = 2\mathbf{k} - \mathbf{k}'$ two fully resonant t -line contributions to $\rho_{mg}^{(3)}(t)$,

$$\begin{aligned}
D_1 &= -i\Lambda \int_{-\infty}^t dt_3 \int_{-\infty}^{t_3} dt_2 \int_{-\infty}^{t_2} dt_1 p(t_3)p^*(t_2 - \tau)p(t_1) \\
& \quad \times e^{i\Delta(t_3 - t_2 + t_1)} e^{-i\omega_{mg}t} e^{-i\omega\tau} e^{-\gamma_{mm}(t_3 - t_2)} e^{-\gamma_{mg}\Phi_t}, \tag{14}
\end{aligned}$$

and

$$\begin{aligned}
D_2 &= -i\Lambda \int_{-\infty}^t dt_3 \int_{-\infty}^{t_3} dt_2 \int_{-\infty}^{t_2} dt_1 p(t_3)p(t_2)p^*(t_1 - \tau) \\
& \quad \times e^{-i\Delta(-t_3 - t_2 + t_1)} e^{-i\omega_{mg}t} e^{-i\omega\tau} e^{-\gamma_{mm}(t_3 - t_2)} e^{-\gamma_{mg}\Phi_t}, \tag{15}
\end{aligned}$$

and two s -line contributions to $\rho_{gm}^{(3)}(s)$,

$$\begin{aligned}
D_1^* &= i\Lambda \int_{-\infty}^s ds_3 \int_{-\infty}^{s_3} ds_2 \int_{-\infty}^{s_2} ds_1 p^*(s_3)p(s_2 - \tau)p^*(s_1) \\
& \quad \times e^{-i\Delta(s_3 - s_2 + s_1)} e^{i\omega_{mg}s} e^{i\omega\tau} e^{-\gamma_{mm}(s_3 - s_2)} e^{-\gamma_{gm}\Phi_s}, \tag{16}
\end{aligned}$$

and

$$\begin{aligned}
D_2^* &= i\Lambda \int_{-\infty}^s ds_3 \int_{-\infty}^{s_3} ds_2 \int_{-\infty}^{s_2} ds_1 p^*(s_3)p^*(s_2)p(s_1 - \tau) \\
& \quad \times e^{i\Delta(-s_3 - s_2 + s_1)} e^{i\omega_{mg}s} e^{i\omega\tau} e^{-\gamma_{mm}(s_3 - s_2)} e^{-\gamma_{gm}\Phi_s}, \tag{17}
\end{aligned}$$

where $\Delta \equiv \omega_{mg} - \omega$, $\Phi_t \equiv t - t_3 + t_2 - t_1$, $\Phi_s \equiv s - s_3 + s_2 - s_1$, and $\Lambda \equiv 2\rho_0(\mu E_0/2\hbar)^3$.

D. The third-order electric polarization

The induced third-order polarization for the dipole-free Bloch two-level system is (for N two-level systems per unit volume)

$$P^{(3)}(t) = N \text{Tr}[\mu \rho^{(3)}(t)] = N\mu[\rho_{gm}^{(3)}(t) + \rho_{mg}^{(3)}(t)]. \tag{18a}$$

The triple-resonance requirement and this particular choice of signal phase (\mathbf{k}_s , not $-\mathbf{k}_s$) excludes the elements $\rho_{gm}(t)$ [and $\rho_{mg}(s)$] at third order [i.e., both D_1 and D_2 are terms in $\rho_{mg}(t)$]:

$$P^{(3)}(t) = N\mu[D_1 + D_2]. \tag{18b}$$

Likewise for the second chromophore,

$$\begin{aligned}
P^{*(3)}(s) &= N \text{Tr}[\mu \rho^{(3)}(s)] = N\mu[\rho_{gm}^{(3)}(s) + \rho_{mg}^{(3)}(s)] \\
&= N\mu[D_1^* + D_2^*]. \tag{19}
\end{aligned}$$

For subsequent stochastic averaging it is analytically advantageous to work in the frequency domain [4,5]. In effect one seeks the monochromatically detected signal intensity at ω_S , $I(\omega_S)$. The signal for any arbitrary slit function (including white detection) can easily be calculated by integrating $I(\omega_S)$ over the appropriate slit function. To pass to frequency space the Fourier transform of the polarization is introduced: $P_t(\omega_S) = \int_{-\infty}^{\infty} dt P(t)e^{i\omega_S t}$ [$P_s^*(\omega_S)$ is just the complex conjugate of $P_t(\omega_S)$ with the t 's replaced by s 's]. The subscripts on the P 's identify their chromophore (time line) origin.

III. STOCHASTIC AVERAGING AND THE SIGNAL

The signal intensity $I(\omega_S)$ requires a classical average at the (bichromophoric) quadrature level over the noise properties of the incoherent fields. That is,

$$I(\omega_S) = \langle |P_s^*(\omega_S)P_t(\omega_S)| \rangle = \left\langle N^2 \mu^2 \int_{-\infty}^{\infty} \int_{-\infty}^{\infty} dt ds e^{i\omega_S t} e^{-i\omega_S s} (D_1^* D_1 + D_1^* D_2 + D_2^* D_1 + D_2^* D_2) \right\rangle. \tag{20}$$

The total signal becomes $I(\omega_S) = N^2 \mu^2 \Lambda^2 (\text{I} + \text{II} + \text{III} + \text{IV})$, where

$$\begin{aligned} \text{I} = & \int d\Omega \langle p^*(s_1)p(s_2-\tau)p^*(s_3)p(t_1)p^*(t_2-\tau)p(t_3) \rangle e^{i\omega_s t} e^{i\omega_s s} e^{-i\omega_{mg}(t-s)} \\ & \times e^{i\Delta(t_3-t_2+t_1)} e^{-i\Delta(s_3-s_2+s_1)} e^{-\gamma_{mm}(t_3-t_2)} e^{-\gamma_{mm}(s_3-s_2)} e^{-\gamma_{mg}\Phi_t} e^{-\gamma_{mg}\Phi_s}, \end{aligned} \quad (21)$$

$$\begin{aligned} \text{II} = & \int d\Omega \langle p^*(s_1)p(s_2-\tau)p^*(s_3)p^*(t_1-\tau)p(t_2)p(t_3) \rangle e^{i\omega_s t} e^{-i\omega_s s} e^{-i\omega_{mg}(t-s)} \\ & \times e^{-i\Delta(-t_3-t_2+t_1)} e^{-i\Delta(s_3-s_2+s_1)} e^{-\gamma_{mm}(t_3-t_2)} e^{-\gamma_{mm}(s_3-s_2)} e^{-\gamma_{mg}\Phi_t} e^{-\gamma_{mg}\Phi_s}, \end{aligned} \quad (22)$$

$$\begin{aligned} \text{III} = & \int d\Omega \langle p(s_1-\tau)p^*(s_2)p^*(s_3)p(t_1)p^*(t_2-\tau)p(t_3) \rangle e^{i\omega_s t} e^{-i\omega_s s} e^{-i\omega_{mg}(t-s)} \\ & \times e^{i\Delta(t_3-t_2+t_1)} e^{i\Delta(-s_3-s_2+s_1)} e^{-\gamma_{mm}(t_3-t_2)} e^{-\gamma_{mm}(s_3-s_2)} e^{-\gamma_{mg}\Phi_t} e^{-\gamma_{mg}\Phi_s}, \end{aligned} \quad (23)$$

$$\begin{aligned} \text{IV} = & \int d\Omega \langle p(s_1-\tau)p^*(s_2)p^*(s_3)p^*(t_1-\tau)p(t_2)p(t_3) \rangle e^{i\omega_s t} e^{-i\omega_s s} e^{-i\omega_{mg}(t-s)} \\ & \times e^{-i\Delta(-t_3-t_2+t_1)} e^{i\Delta(-s_3-s_2+s_1)} e^{-\gamma_{mm}(t_3-t_2)} e^{-\gamma_{mm}(s_3-s_2)} e^{-\gamma_{mg}\Phi_t} e^{-\gamma_{mg}\Phi_s}. \end{aligned} \quad (24)$$

We have defined the eightfold time integration as

$$\int d\Omega \equiv \int \int_{-\infty}^{\infty} dt ds \int_{-\infty}^s ds_3 \int_{-\infty}^{s_3} ds_2 \int_{-\infty}^{s_2} ds_1 \int_{-\infty}^t dt_3 \int_{-\infty}^{t_3} dt_2 \int_{-\infty}^{t_2} dt_1.$$

for short. Equations (21)–(24) reveal the four distinct six-point time correlators involving the stochastic noise function central to the problem. (Were we to have included those terms that do not exhibit full resonance there would have been altogether nine different six-point correlators.)

A. Stochastic averaging

The terms I, II, III, and IV above are complicated by the otherwise unresolved six-point time correlators. To proceed, we assume complex circular Gaussian statistics [14] and stationarity, though recent work shows how for certain experimental situations (high optical density or very intense fields) both complex circular Gaussian statistics and stationarity do not hold [15]. Accordingly, the present treatment will not apply to such conditions. The complex Gaussian moment theorem [14] is introduced to express any given six-point correlator as a sum of six terms each consisting of a product of three two-point correlators. This breakdown of each of the present four six-point correlators is shown explicitly in Appendix A. The two-point correlators, of course, are significantly easier to handle analytically. It is significant to note how, given stationarity, each of the six-point correlators

breaks into four terms having (two) τ -dependent two-point correlators and two terms having no τ dependence.

B. Outline of the analytic calculation aided by computer

At this point, enumeration of the terms requiring analytic treatment reveals a total of 24, six each from the intensity level integrals I, II, III, and IV. The six are designated a, b, c, d, e, and f (see Appendix A). Of the 24, 16 terms exhibit τ dependence. Only these can be responsible for the interesting interferometric properties of the signal though the τ -independent contribution is also informative as a constant background term. Analytic results have been obtained for each of the 16 τ -dependent terms using, for analytic convenience, a Lorentzian spectral density for the noisy light. Now the two-point correlator becomes $\langle p(a)p^*(b) \rangle = \langle p(a-b)p^*(0) \rangle = e^{-\Gamma|a-b|}$, where $\Gamma \equiv 1/\tau_c$. As it turns out, the essential absolute value for the time interval in this correlation function presents a significant problem for direct time-domain integration. To avoid this issue the Wiener-Khintchine theorem [16] is introduced to express every two-point correlator as an integral over the spectral density J , $\langle p(x)p^*(0) \rangle = \int_{-\infty}^{\infty} J(q)e^{iqx} dq$. In this case the spectral density is Lorentzian. Thus each of the 16 τ -dependent terms (I–IV, a–d) is finally expressed in generic form as

$$\begin{aligned} (\text{term}) = & N^2 \mu^2 \Lambda^2 \int d\Omega \int_{-\infty}^{\infty} dq_1 \int_{-\infty}^{\infty} dq_2 \int_{-\infty}^{\infty} dq_3 J(q_1)J(q_2)J(q_3) \\ & \times e^{iq_1(\eta_1)} e^{iq_2(\eta_2)} e^{iq_3(\eta_3)} e^{-i\Delta(\kappa)} e^{-\gamma_{mm}(t_3-t_2+s_3-s_2)} e^{-\gamma_{mg}(\Phi_t-\Phi_s)} e^{-i\omega_{mg}(t-s)} e^{i\omega_s(t-s)}, \end{aligned} \quad (25)$$

TABLE I. Time variables in the exponents of generic Eq. (25).

Term	κ	η_1	η_2	η_3
I a	$-(t_3-t_2+t_1)+(s_3-s_2+s_1)$	$s_2-s_1-\tau$	$t_1-t_2+\tau$	t_3-s_3
I b	$-(t_3-t_2+t_1)+(s_3-s_2+s_1)$	$s_2-s_3-\tau$	$t_1-t_2+\tau$	t_3-s_1
I c	$-(t_3-t_2+t_1)+(s_3-s_2+s_1)$	$s_2-s_1-\tau$	$t_3-t_2+\tau$	t_1-s_3
I d	$-(t_3-t_2+t_1)+(s_3-s_2+s_1)$	$s_2-s_3-\tau$	$t_3-t_2+\tau$	t_1-s_1
II a	$+(-t_3-t_2+t_1)+(s_3-s_2+s_1)$	$s_2-s_1-\tau$	$t_2-t_1+\tau$	t_3-s_3
II b	$+(-t_3-t_2+t_1)+(s_3-s_2+s_1)$	$s_2-s_3-\tau$	$t_2-t_1+\tau$	t_3-s_1
II c	$+(-t_3-t_2+t_1)+(s_3-s_2+s_1)$	$s_2-s_1-\tau$	$t_3-t_1+\tau$	t_2-s_3
II d	$+(-t_3-t_2+t_1)+(s_3-s_2+s_1)$	$s_2-s_3-\tau$	$t_3-t_1+\tau$	t_2-s_1
III a	$-(t_3-t_2+t_1)-(-s_3-s_2+s_1)$	$s_1-s_2-\tau$	$t_1-t_2+\tau$	t_3-s_3
III b	$-(t_3-t_2+t_1)-(-s_3-s_2+s_1)$	$s_1-s_3-\tau$	$t_1-t_2+\tau$	t_3-s_2
III c	$-(t_3-t_2+t_1)-(-s_3-s_2+s_1)$	$s_1-s_2-\tau$	$t_3-t_2+\tau$	t_1-s_3
III d	$-(t_3-t_2+t_1)-(-s_3-s_2+s_1)$	$s_1-s_3-\tau$	$t_3-t_2+\tau$	t_1-s_2
IV a	$+(-t_3-t_2+t_1)-(-s_3-s_2+s_1)$	$s_1-s_2-\tau$	$t_2-t_1+\tau$	t_3-s_3
IV b	$+(-t_3-t_2+t_1)-(-s_3-s_2+s_1)$	$s_1-s_3-\tau$	$t_2-t_1+\tau$	t_3-s_2
IV c	$+(-t_3-t_2+t_1)-(-s_3-s_2+s_1)$	$s_1-s_2-\tau$	$t_3-t_1+\tau$	t_2-s_3
IV d	$+(-t_3-t_2+t_1)-(-s_3-s_2+s_1)$	$s_1-s_3-\tau$	$t_3-t_1+\tau$	t_2-s_2

where each of the 16 sets of η_1 , η_2 , η_3 , and κ is listed in Table I. At this point an algorithm was set up on the commercial symbolic algebra software program MATHEMATICA [17] to organize and expedite the analytic solution. The lengthy calculations are not presented in explicit detail.¹ Rather, the steps performed by the MATHEMATICA algorithm are outlined. First the order of integration in Eq. (25) was changed such that the time integrals in $\int d\Omega$ were performed first (excluding the integrals over s and t). Next the change of variables $t=t$, $\xi=t-s$ [18] was introduced to isolate an integral representation of the δ function using the integral over ξ . This δ function aids in performing one of the q integrations (we chose q_3). The remaining two q integrations were carried out using analytic continuation and contour integration in the complex q plane and the theory of residues. The residues were collected according to the positive and negative τ for each term and plotted as we shall see later. Since from the start Euler's relation has been used to express the field as the sum of complex functions in the usual way, the physical (real) I⁽³⁾D4WM signal is given as the real part of the above analytic result.

IV. THE FACTORIZED TIME CORRELATION DIAGRAMS

The lengthy calculations required may be greatly organized and in fact ultimately circumvented by the use of a diagrammatic technique now introduced. Diagrams may be constructed directly from each and every triplet of two-point correlators appearing in the breakdown of the six-point correlators. These diagrams are called factorized time correlation (FTC) diagrams. Once the analytic solution is obtained for the signal interferogram for each of the 16 FTC diagrams, simple rules may be discerned that duplicate the analytic result in the limit of zero detuning ($\omega_{mg} = \omega = \omega_s$). The rules

for the case of nonzero detuning become complicated to the point where they are of little use. In any case, for white detection the I⁽³⁾D4WM signal is strongly quenched by detuning oscillations ($\omega_{mg} \neq \omega$). Not only do the FTC diagrams recover the proper analytic result, but they yield much insight into the physics of the problem. The rules for their construction and for obtaining the analytic signal from them are discussed in detail in Appendix B.

In general there is a defined correspondence between any given term composing the signal and its FTC diagram, i.e., one can draw a diagram for each of the 24 triplets of two-point (pair) correlators. A FTC diagram consists of a template of s and t time lines each with a tick that marks the time of each of the three field interventions. Superimposed are *segments* (arrows or lines) which link the times contained in each two-point correlator. A τ -dependent pair correlator is represented by an *arrow* segment always pointing to the tick mark corresponding to the action of field F' . A τ -independent pair correlator is represented by a *line* segment connecting the two times contained in the pair correlator. Clearly, from the standard definition of a pair correlator the contribution to the total signal from all FTC diagrams that contain one or more arrows must vanish as $\tau \rightarrow \infty$. On the other hand, at $\tau=0$ all arrows turn into lines. Our I⁽³⁾D4WM problem has 16 FTC diagrams that contain two arrows and one line each. These represent the τ -dependent terms. Significantly, in the present problem the arrows never connect the two time lines, while the line always does (for the I⁽³⁾D4WM spectroscopy being considered). In other spectroscopies arrows can connect the two time lines and, as will be argued in Sec. V, such FTC diagrams will make relatively weak contributions to the τ -dependent signal of those spectroscopies. The eight remaining (τ -independent) FTC diagrams consist of three lines where each links the two time lines.

A. The τ -dependent part of the signal

The 16 τ -dependent FTC diagrams, arranged according to rows I, II, III, and IV, and columns a, b, c, and d, are shown

¹An annotated copy of the calculation algorithm and files of the resulting terms in both MATHEMATICA and TEX formats (both are Windows files) are available from the authors.

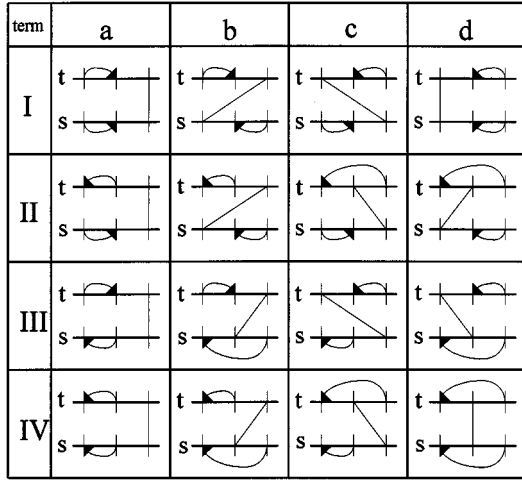


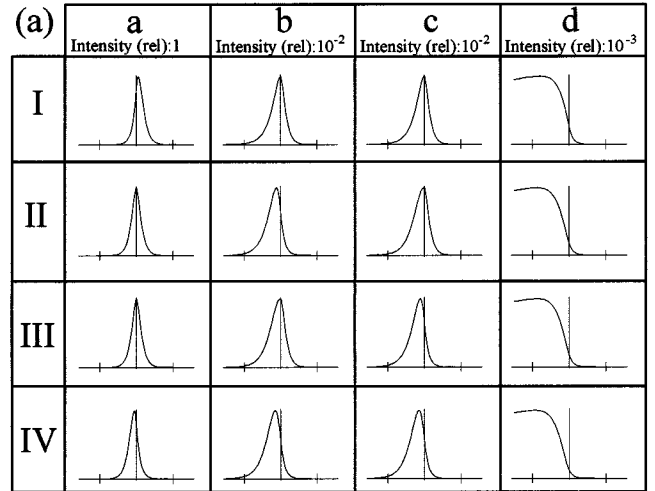
FIG. 3. The 16 τ -dependent FTC diagrams. The rows refer to the four six-point correlators derived from stochastic averaging at the intensity level; the columns refer to the four τ -dependent triplets of pair correlators generated from the breakdown of the six-point correlators by use of the complex Gaussian moment theorem (see text for details). The columns are arranged in decreasing order of their (anticipated) interferogram intensities as they contribute to the total $I^{(3)}$ D4WM signal. Each tick mark represents the time when there is a field intervention ($t_1 < t_2 < t_3$; $s_1 < s_2 < s_3$; time increases from left to right).

in Fig. 3. (The columns are intentionally ordered such that the relative strength of their contribution to the total signal decreases from a to d for parameters $\tau_c \approx T_2 \ll T_1$.) Important features of the FTC diagrams in Fig. 3 are (i) no arrows link the t line and s line, that is, the τ dependence is only *intrachromophoric*; (ii) all lines link the t line and s line, that is, the τ -independent pair correlator is completely *interchromophoric*; (iii) in no diagram do arrow heads point to t_3 or s_3 (F' cannot appear last); (iv) in column a time points t_3 and s_3 involve only lines; and (v) in column d two points t_3 and s_3 involve only arrow tails.

The analytic results shown graphically (Figs. 4–7) reveal additional patterns for four distinct sets of the parameters (τ_c, T_1, T_2). Although the analytic solution for any parameter set is in hand, we have displayed the interferograms only for zero detuning. The peak intensity of the plots in column a of Fig. 4(a) is arbitrarily set to magnitude 1 and the relative order-of-magnitude scaling for all other columns is indicated in their heading. (Figure 7 shows only the total interferogram.)

1. Parameter set $\tau_c \approx T_2 \ll T_1$

Figure 4(a) shows plots of the signal contributions for a “typical” set of parameters; namely, a short correlation time of the light, rapid dephasing rate, and a relatively long excited-state lifetime. The intensity decreases dramatically from column a to d. Asymmetric shapes can be found, some even showing peaks shifted from $\tau = 0$. These presumably unintuitive peak shifts correspond to diagrams having the two arrows pointing in the same direction. A striking feature is seen in column d. Though relatively weak, the signal is highly one sided, its peak significantly shifted from $\tau = 0$,



(b)

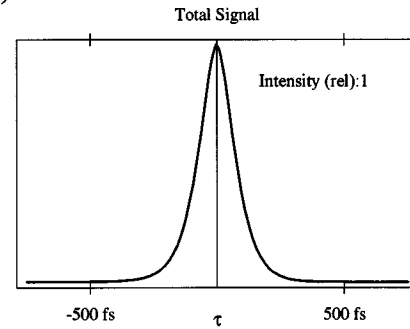


FIG. 4. (a) $I^{(3)}$ D4WM interferograms for each of the 16 FTC diagrams (Fig. 3) to the total $I^{(3)}$ D4WM signal versus τ . Abscissa: tick marks at $\tau = \pm 500$ fs. Parameters: $\tau_c = 100$ fs, $T_1 = 10$ ps, $T_2 = 50$ fs, and zero detuning. The relative intensity (ordinate) is similar for every FTC diagram within each column. The relative intensity across columns is indicated by the scaling factor in their headings. (b) The corresponding total $I^{(3)}$ D4WM interferogram.

and it decays relatively slowly. Such a pattern is derived from diagrams in which the time points t_3 and s_3 involve arrow tails. So in column d all relatively slow decay (associated with a long T_1) appears only for negative τ . This important feature was first realized by inspection of the analytic expression for the FTC diagrams. Figure 4(b) shows the total interferogram. Its shape is dominated by the sum of contributions from column a which have a combination of the rapid decay due to material dephasing (T_2) and the loss of good interferometric overlap of F and F' (τ_c). The long tail (due to T_1) for negative τ is much weaker (roughly 1000 times weaker than the peak intensity) and is not noticeable in the figure. Thus the total $I^{(2)}$ D4WM signal is very nearly symmetric about $\tau = 0$.

2. Parameter set $\tau_c \ll T_2 \ll T_1$

The graphs in Fig. 5 represent analytic results for the parameter set in which the coherence time of the light is made ultrashort, the dephasing time remains short, and the lifetime remains relatively long. Thus shortening τ_c reduces the intensity significantly across all columns (relative to Fig.

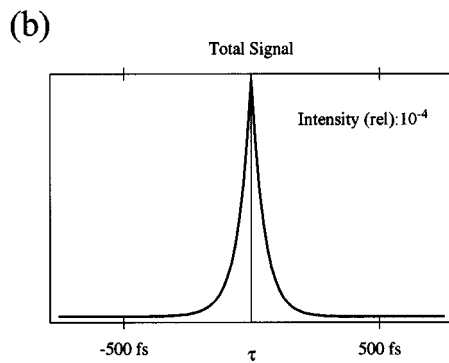
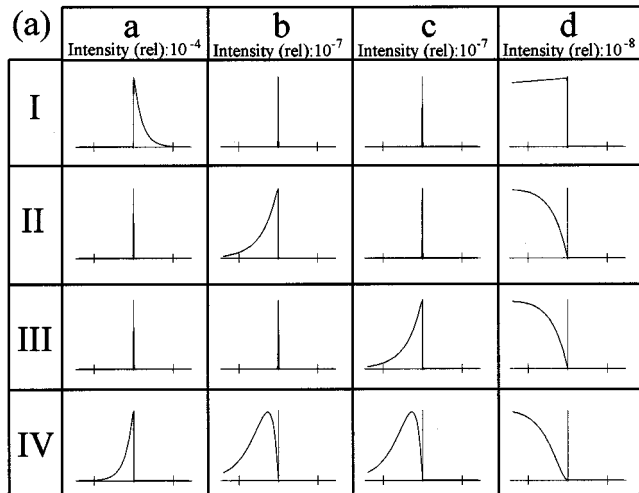


FIG. 5. Same as Fig. 4 except with tick marks at $\tau = \pm 250$ fs. Parameters: $\tau_c = 1$ fs, $T_1 = 10$ ps, $T_2 = 100$ fs, and zero detuning. The relative intensity scaling (in column heading) is with reference to column a of Fig. 4. This parameter set approaches a white-noise (δ -function autocorrelation) limit for the noisy light.

4). A subset of six (I b and c; II a and c; III a and b) graphs recognizes the very rapid decay associated only with the light and essentially does not reflect the longer times T_2 or T_1 of the two-level system. The common feature of these six FTC diagrams is that they are the only ones with oppositely pointing arrows (see Fig. 3). The total signal [Fig. 5(b)] contains a very slight asymmetry (not noticeable in the figure) since at negative τ (only) the signal holds up slightly due to the long lifetimes in the parameter set. The rapid decay of the total signal is again governed by the sum of column a which is now almost exclusively due to dephasing (T_2). Because of this dominance, the total interferogram appears symmetric.

3. Parameter set $T_2 \ll \tau_c \ll T_1$

Figure 6 represents another limiting case. Now the dephasing is made ultrashort, the correlation time short, and the lifetime relatively long. Once more there is an overall marked decrease in the strength of the signal (relative to Fig. 4). The loss of coherence memory in the two-level system has quenched the 4WM signal for every FTC diagram. Regarding shape, the most striking feature is that the four plots within each column have become identical. Also, the graphs in column a (still dominant) are symmetrical while the others are not. None of the dominant diagrams of column a carry

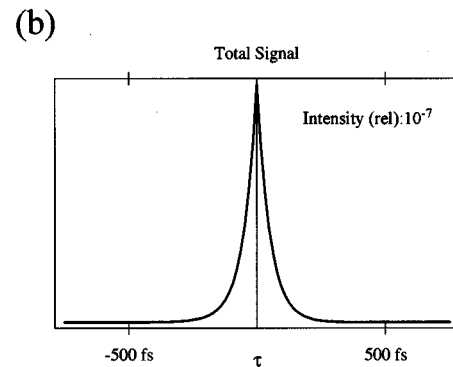
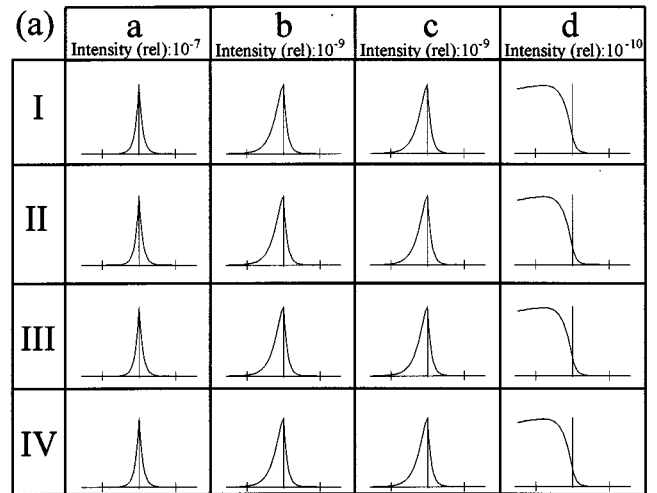


FIG. 6. Same as Fig. 4 except with parameters $\tau_c = 100$ fs, $T_1 = 10$ ps, $T_2 = 1$ fs, and zero detuning. The relative intensity of the interferograms is in reference to that of column a of Fig. 4. These parameters approach a zero-memory limit.

τ -dependent lifetime information, whereas the other diagrams do to some degree, although their contribution is relatively much weaker. Thus the total signal [Fig. 6(b)] is essentially symmetrical and decays principally according to τ_c . The slower decay due to T_1 (for $\tau < 0$ only) remains roughly 1000 times weaker than the peak intensity, thus giving the signal slight asymmetry (not noticeable in the figure) upon close inspection.

4. Parameter set $\tau_c \approx T_2 \approx T_1$

Figure 7 shows the total interferogram found for the case in which the lifetime is made very short, i.e., on the order of the other parameters. (The individual FTC interferograms are not shown.) This parameter set approaches the limit in which pure dephasing (T_2') becomes small. The shortening of T_1 weakens column a to the point where column d, with dramatic asymmetries that include peak shifts, is of comparable strength. Under these conditions the total signal is asymmetric with a peak significantly shifted from $\tau = 0$. The rapid decay seen in the total interferogram is now a combination of all three (T_1, T_2, τ_c) system parameters.

In Table II column by column relative intensities are listed for other interesting parameter sets. Tables III, IV, and V list the ratios of the $\tau = 0$ magnitudes among the columns in

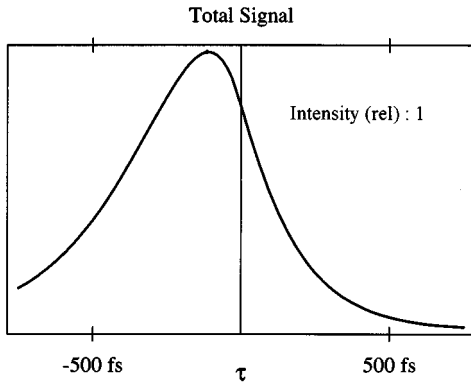


FIG. 7. The total $I^{(3)}$ D4WM interferogram for the parameters $\tau_c = 100$ fs, $T_1 = 400$ fs, $T_2 = 300$ fs, and zero detuning. The relative intensity is in reference to that of column a of Fig. 4. This parameter set approaches a short-lifetime (and short-pure-dephasing-time) limit. The potential for a peak shift to nonzero τ is dramatically exposed.

terms of the parameters for the three different limiting cases, respectively, $\tau_c \approx T_2 \ll T_1$, $\tau_c \ll T_1$, and $T_2 \ll \tau_c \ll T_1$.

B. The τ -independent part of the signal

The eight remaining (τ -independent) FTC diagrams of the 24 are shown in Fig. 8. These obviously consist of only straight lines. In each case all three pair correlators are *interchromophoric*. There appear to be three types of diagrams with respect to the number of times the lines are crossed. There are diagrams with no crossed lines, two crossed lines, and all three lines crossed.

The increase from only one interchromophore coupling in the 16 τ -independent diagrams to three in the eight τ -independent diagrams is in some sense a fundamental difference between these two important classes of diagrams. As a result, the same rules derived from the analytic results for the τ -dependent diagrams cannot be carried over to the τ -independent diagrams. The many interesting consequences of these patterns will be discussed next.

V. PHYSICAL INTERPRETATION

The noisy nature of the light which is vital to all incoherent light spectroscopies blurs the physical picture of the underlying mechanisms that make up this interesting area of physics. Not only does a new layer of analytic challenge appear, but more exciting is the challenge to clarify the physical aspects of the treatment. It appears that (for station-

TABLE II. Two-beam $I^{(3)}$ D4WM relative intensities for several material and light parameter sets.

τ_c (fs)	T_2 (fs)	T_1 (ps)	a	b	c	d
100	300	10	10^2	1	1	10^{-1}
100	50	10	1	10^{-2}	10^{-2}	10^{-3}
100	1	10	10^{-7}	10^{-9}	10^{-9}	10^{-10}
1	200	0.6	10^{-7}	10^{-7}	10^{-7}	10^{-7}
1	200	10^4	10^2	10^{-2}	10^{-2}	10^{-7}

TABLE III. Relative intensity of FTC interferograms (at $\tau=0$) in terms of the reduced dephasing time and reduced correlation time for the limiting case where $T_1 \gg T_2 \approx \tau_c$ and zero detuning. The reduced times are generically defined as $T \equiv O(\tau_c/T_1) \approx O(T_2/T_1)$.

Term	a	b	c	d
I	1	T	T	T^2
II	1	T	T	T^2
III	1	T	T	T^2
IV	1	T	T	T^2

arity and complex Gaussian statistics) the FTC diagrams represent elementary physical components of incoherent light spectroscopies in general and the present $I^{(3)}$ D4WM in particular. That is, the FTC diagrams represent terms in the analytic expression for the total signal that appear to have elementary physical interpretation. Any further breakdown of the analytic expression would seem to lose such physical meaning. We now seek a more revealing understanding of the FTC diagrams.

A. Some conceptual tools

The wide variety of shapes seen among individual τ -dependent FTC interferograms as they contribute to the total $I^{(3)}$ D4WM interferogram is striking. Perhaps even more remarkable are the very different relative signal intensities across columns for any given parameter set and the strikingly different overall relative intensities among the different parameter sets (cf. the column headings in Figs. 4–6). In order to rationalize these features along with other more subtle points, it is helpful to develop several conceptual tools.

term	e	f
I		
II		
III		
IV		

FIG. 8. The eight τ -independent FTC diagrams for $I^{(3)}$ D4WM. As in Fig. 3 the rows refer to the four six-point correlators in the response function at the intensity level and the columns refer to the (two) τ -independent terms derived from the breakdown of each of the six-point correlators (see text for details).

The first of these tools involves the nature of the light. The electric field from the light forms a random pattern as a function of time. One might call this its “fingerprint.” Now, for any given nanosecond light pulse F' will have exactly the same “fingerprint” as F , only it is shifted by τ . When this time shift is within the coherence time of the light, the twin beams recognize that they are from the same source. Overlap of the beams results in high interferometric contrast (i.e., strong constructive and also strong destructive interference) as long as $|\tau| < \tau_c$. Equivalently, if one were to examine the “fingerprint” of the beam F around some moment in time t_0 (measured from a laboratory reference) one would find the identical “fingerprint” region in beam F' at $t_0 - \tau$. Were beam F to perturb the system at t_0 then the “preferred” time giving the concerted action of twin F' would be the region around $t_0 - \tau$ for optimal interferometric contrast. This region is designated the “preferred” region.

The second conceptual tool involves the time symmetry of the elementary components (here referring to the light and the material response) of the I⁽³⁾D4WM interferogram. The time symmetry of the noisy field is rooted in the nature of the “preferred” region. The preferred region has *two-sided time symmetry*. In other words, if F happened to have acted upon a chromophore at laboratory time t_0 then the “preferred” time for F' to join in concerted action is centered around $t_0 - \tau$ such that action at $(t_0 - \tau) - \epsilon$ (where ϵ is a time $< \tau_c$) is equally “preferred” to action at $(t_0 - \tau) + \epsilon$. By contrast, in this same sense the material response function of the chromophore has *one-sided time symmetry*. In the Bloch two-level system one encounters a simple coherence response and a population response. First, a field action at time t_1 on the chromophore in the ground state (the first field intervention) may cause an electronic polarization which subsequently will decay with a dephasing rate constant γ_{mg} . Secondly, a second field intervention can build on this polarization to create an excited-state population which then will decay with rate constant γ_{mm} . Both events have one-sided time symmetry. If the first field acts on the chromophore at time t_1 then at $t_1 - \epsilon$ there is no polarization while at time $t_1 + \epsilon$ there is a polarization. Likewise, if the second field acts at t_2 then at $t_2 - \epsilon$ there is only a polarization (assume $\epsilon < T_2$) but at $t_2 + \epsilon$ there is a population.

Still another important conceptual tool is that of the freedom to “slide along a time line” (to “accumulate” or to “integrate”). Since F and F' are “always” present, any time intervention (tick mark on the FTC diagrams) or pair of interventions, is free to slide along the time line provided that both the integrity of the 4WM signal is preserved and the specific time ordering associated with a given diagram is maintained. To “slide along the time line” indicates the potential for field action to take place at any time over which the tick mark is permitted to slide. However, an individual tick mark is locked to a partner tick mark by the segment (arrow or line) representing a pair correlator. The two tick marks, thus linked, correspond to a correlated event pair that must slide along the time line together.

The final conceptual tool is concerned with the event coupling between the two time lines (t and s). This coupling obviously involves interchromophoric pair correlators (lines). It has been noted how all of the τ -independent correlators in our I⁽³⁾D4WM experiment are depicted by lines

TABLE IV. Relative intensity of FTC interferograms (at $\tau=0$) in terms of the reduced dephasing time and reduced correlation time ($\bar{\tau}_c \equiv \tau_c/T_1$, $\bar{T}_2 \equiv T_2/T_1$) for the limiting case of white noise ($\tau_c \rightarrow 0$) and zero detuning.

Term	a	b	c	d
I	1	\bar{T}_2	\bar{T}_2	\bar{T}_2^2
II	1	\bar{T}_2	$\bar{\tau}_c$	$\bar{\tau}_c \bar{T}_2$
III	1	$\bar{\tau}_c$	\bar{T}_2	$\bar{\tau}_c \bar{T}_2$
IV	1	$\bar{\tau}_c$	$\bar{\tau}_c$	$\bar{\tau}_c \bar{T}_2$

that happen to be only interchromophore. These correspond to the correlated action of F with itself and F' with itself. This implies tight synchronization between the two chromophores of the events linked by a given correlator line. The “precision” or “strength” of this synchronization is proportional to τ_c (the interferometric width of the “preferred” region). All arrows are intrachromophore (and correlate F to F') and themselves contain no interchromophoric synchronization. An arrow on one chromophore is oblivious to the timing of events on the second chromophore.

We now are ready to rationalize the I⁽³⁾D4WM FTC signals with regard to both their remarkable range of relative intensities and the great variety of shapes displayed among their interferograms.

B. Intensity

We limit our focus to the τ -dependent diagrams. First, the lone interchromophore pair correlator (line) found in each FTC diagram synchronizes the t and s time lines to within τ_c . Beyond this synchronization, the two intrachromophore pair correlators (arrows) in each FTC diagram are free to independently slide anywhere on the time line (to accumulate signal strength) provided the integrity of the third-order process is maintained. This will explain the relative intensity differences among the different columns as well as that among different parameter sets.

In examining the FTC diagrams of column a in Fig. 3, one sees how events at t_1 and t_2 (along with those at s_1 and s_2) form single-time-line correlated pairs (they are connected by arrows). These two event pairs may slide (independently) along their respective time lines. However, to preserve 4WM integrity this sliding must be confined to the approximate time interval $t_3 - T_1$ up to t_3 (and $s_3 - T_1$ up to s_3). Had the pair acted prior to $t_3 - T_1$ (or $s_3 - T_1$) the 4WM signal would have ceased since the induced population would have collapsed by the time the last field acted at t_3 . It follows that the

TABLE V. Relative intensity of FTC interferograms (at $\tau=0$) in terms of the reduced correlation time ($\bar{\tau}_c \equiv \tau_c/T_1$) for the limiting case of zero material memory ($T_2 \rightarrow 0$) and zero detuning.

Term	a	b	c	d
I	1	$\bar{\tau}_c$	$\bar{\tau}_c$	$\bar{\tau}_c^2$
II	1	$\bar{\tau}_c$	$\bar{\tau}_c$	$\bar{\tau}_c^2$
III	1	$\bar{\tau}_c$	$\bar{\tau}_c$	$\bar{\tau}_c^2$
IV	1	$\bar{\tau}_c$	$\bar{\tau}_c$	$\bar{\tau}_c^2$

longer the lifetime (T_1) the larger is column a's contribution to the signal. This is consistent with the trend seen among the parameter sets presented above (cf. rows 4 and 5 of Table II). In contrast to the diagrams of column a, diagram I d has its single-time-line correlated event pairs at t_2 and t_3 and at s_2 and s_3 . To maintain the integrity of the 4WM signal these pairs must limit their sliding to the time interval t_1 to $t_1 + T_2$ (s_1 to $s_1 + T_2$). Whenever $T_2 < T_1$ this accumulation interval is smaller than that enjoyed by column a and their contribution to the total intensity is correspondingly weaker. This is confirmed by the indicated relative signal strengths in the column headings in Figs. 4–6 as well as those shown in Table II. Diagram IV d has single-chromophore correlated pair events at t_1 and t_3 and at s_1 and s_3 . Now the time interval over which these pairs may slide is less well defined since τ_c and T_2 (and T_1 as well) are entangled, for the t_2 (s_2) intervention is straddled by these two single-time-line pair correlators. With regard to the relative intensity, diagram IV d is on the order of diagram I d (but their two shapes may be quite different as we shall see). The remaining FTC diagrams of column d, II d and III d, are of the same order of magnitude as I d and IV d since they contain comparable event correlators.

Columns b and c in a sense contain event correlation that is a hybrid between those seen in column a and those in column d. As might be expected their relative intensity contribution is similar and always lies between those of columns a and d.

C. Shape

We turn towards a rationalization of the observed shapes of the analytic contributions from each of the 16 τ -dependent FTC diagrams to the final I⁽³⁾D4WM interferogram. In particular the correspondence between the directions of the arrows and the peak shift from $\tau=0$ seen along the asymmetrically shaped interferograms is explained.

A right-pointing arrow necessarily indicates the action of F' following that of F . Such a correlated event pair is *most* active in the 4WM process when $\tau > 0$. The reason it is not exclusively active only for $\tau > 0$ is due to the finite, nonzero width of the “preferred” region. Likewise, a left-pointing arrow necessarily obliges F to follow F' . This event pair is most active when $\tau < 0$. Thus those nine FTC diagrams in which both (s -line and t -line) arrows point to the left (all column d diagrams, all row IV diagrams, II b, and III c) are active at negative τ but quickly vanish (with rate constant $1/\tau_c$) for positive τ . Accordingly, their interferograms must be variously asymmetric and shifted towards the left. The one and only FTC diagram in which both arrows point to the right (I a) is active at positive τ and must quickly vanish (with rate constant $1/\tau_c$) for negative τ . Its interferogram must be asymmetric and shifted towards the right. The remaining six FTC diagrams (I b and c; II a and c; III a and b) contain two oppositely pointing arrows, as already noted. Their signal contributions must be quenched for both positive and negative τ to produce interferograms that are relatively symmetric and peaked at $\tau=0$.

These patterns are more or less conspicuous in the graphs across Figs. 4–6, but most pronounced in Fig. 5 where $\tau_c \ll T_2 \ll T_1$. For all the striking asymmetry among the FTC

graphs in Fig. 5, the total signal is essentially symmetric because column a dominates and right-pointing I a adds to left-pointing VI a to produce a symmetric result whose two-sided decay basically represents dephasing dynamics. There are parameter sets where τ_c is very short but in which there is a pronounced asymmetry in the total signal. This is the case when T_2 and T_1 are of similar order of magnitude. Row 4 of Table II is one such parameter set.

These general patterns are less obvious in Fig. 6 where $T_2 \ll \tau_c \ll T_1$. Now column a still dominates because T_2 remains much shorter than T_1 . Since T_2 is so short the distinction between right-pointing and left-pointing pair correlation is (in this case strongly) suppressed and it is the size of the “preferred” region that now determines the shape. Strikingly, throughout the parameter space (Figs. 4–6) column d remains highly left asymmetric, so much so that its peak appears at relatively large negative τ .

These asymmetries and peak shifts for those ten FTC diagrams having common pointing arrows can be explained by arguing that the largest contribution to the graph of a particular FTC diagram occurs when the two-sided “preferred” region enjoys maximum overlap with the one-sided material response (coherence loss or lifetime decay). Thus the optimal delay τ for any given arrow is not when F and F' are exactly contemporary (at $\tau=0$) but is when F' leads (lags behind) F for right- (left-) pointing arrows. It is then when *both sides* of the “preferred” region achieve maximum overlap with the one-sided response function of the two-level system. This point is illustrated in Fig. 9 for the t line of diagram I a. A similar picture (with the necessary modifications) holds for all time lines having their single-time-line pair correlators on adjacent tick marks. Essentially a function that has two-sided time symmetry is being convolved with a function that has one-sided time symmetry. This forces a nonzero τ for the peak of the signal. This effect is normally most conspicuous for the column d diagrams since there all arrows have tails at the last intervention and the population decay rate constant γ_{mm} is often much smaller than the other rate constants. The peak shift τ_{\max} from zero from diagram I d is nearly τ_c . More quantitatively, in the limit of $T_1 \rightarrow \infty$, then $\tau_{\max} \rightarrow \tau_c$. The off-center locations of the peaks for the other three shifted diagrams in column d are complicated by the influence of the dephasing rate constant. In full generality the peak position must be found numerically. This role of the dephasing rate constant in the graphs of II d, III d, and IV d is evident when in Fig. 5 (very short τ_c) it is seen how while I d peaks very near $\tau=0$, II d, III d, and IV d remain strongly shifted. Only I d contains no event pair correlators that straddle the second intervention.

As when dealing with the relative intensities, those diagrams having arrows that straddle T_2 or s_2 , thus connecting t_1 and t_3 or s_1 and s_3 (II c, II d, III b, III d, IV b, IV c, and IV d), are somewhat less intuitive. For this case the role of the straddled intervention (at t_2 or s_2) not directly involved with the τ dependence becomes more evident (though its synchronization role is present in every FTC diagram). Here field F' excites a polarization at time t_1 . While the polarization is still significant, the field F acts at t_2 to create a population, but it is not correlated to the action of F or F' at t_1 or t_2 and the “preferred” region argument does not apply. Nevertheless, the action of F at t_2 must occur prior to the second

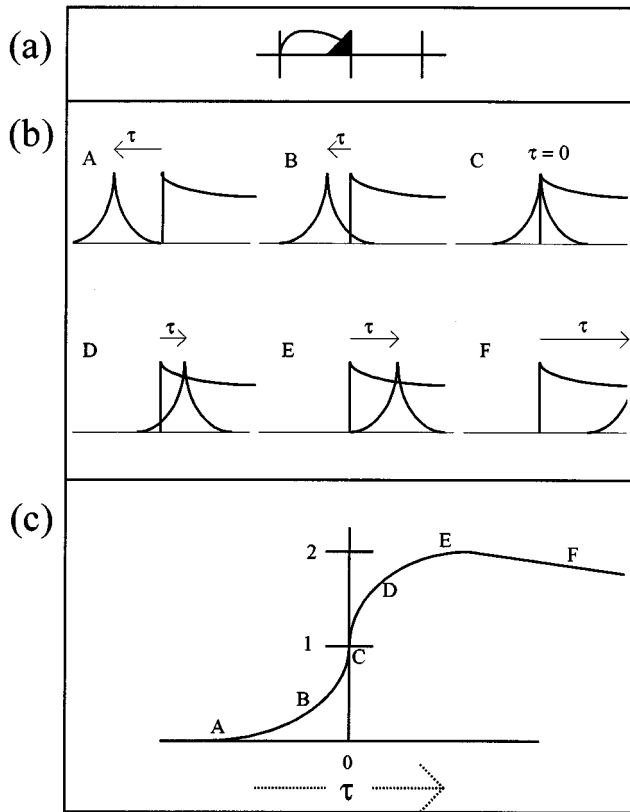


FIG. 9. Modeling of the peak shift from $\tau=0$. (a) A τ -dependent event pair correlator between the first two steps of 4WM. (b) Illustration of the “preferred” portion of the noisy light having *two-sided time symmetry* to be convolved with the material response function (in this case showing electronic coherence decay) having *one-sided time symmetry* for six different τ settings. (c) The resulting convolution. The peak at nonzero τ (E) is evident.

action of F (at time t_3) which is optimized by use of the “preferred” portion of the light (time t_3 is correlated to the action at time t_1). Thus the later this final intervention at t_3 is after that of t_1 the more opportunity there is for the middle τ -independent intervention to accumulate and to yield a stronger signal. Yet the last intervention must not be so late as to lose the benefit of the “preferred” action of the correlated first and third field interventions. Here, as with the “adjacent” case, it is advantageous for F' to lead F ($\tau < 0$). (The straddle cases only involve left-pointing arrows.) Thus their strongest contribution occurs at negative τ . It is helpful to compare and contrast the two extreme parameter sets, one with near-zero τ_c (Fig. 5) and the other with near-zero T_2 (Fig. 6). Particularly examine column d in the two cases. For near-zero T_2 , coherence is lost immediately; thus the second intervention on the s and t lines must coincide in time with the first intervention. For short T_2 all FTC diagrams could be redrawn by making the first two tick marks coincident. When this is done all diagrams in any given column become equal. This is dramatically illustrated in Fig. 6. Conversely with zero τ_c , the “preferred” region now has zero width. The “preferred” region becomes δ -function-like. Plot I d (Fig. 5) shows the expected simple result for a convolution of a δ function and a function with one-sided time symmetry. In contrast diagrams II d, III d,

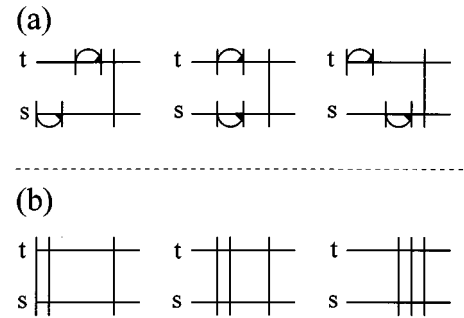


FIG. 10. Rationalizing the large peak-to-background contrast ratio. (a) All τ dependence is *intrachromophoric* (arrows) in the present $I^{(3)}D4WM$ experiment and there is only one t -line- s -line synchronization. The arrow pair events are free to “slide” (accumulate) independently on each time line. None of the τ -independent diagrams are analogs to these. (b) The τ -independent (background) diagrams show three t -line- s -line synchronizations (lines). No independent “sliding” on the t line and on the s line is available. Accumulation is considerably inhibited. See text for more details.

and IV d clearly show the accumulation possible due to the additional freedom available for the intermediate second intervention when T_2 is nonzero.

D. τ -independent terms and the contrast ratio

The τ -dependent terms yield information on all Bloch two-level parameters. Nonetheless it is important to at least qualitatively examine the τ -independent terms. Some of the physical arguments stemming from the τ -dependent diagrams may be applied to the τ -independent diagrams (lines only). These terms are represented by diagrams having three interchromophore pair correlators. This means that there are three t -line- s -line synchronizations which reduce the degree of freedom and greatly weaken the contribution to the signal. Rather than being able to integrate over the lifetime independently for each chromophore, the integration (accumulation) is now simultaneous. The “sliding” is no longer independent on each time line, leading to a great reduction in overall signal strength. Figure 10 compares diagram I a with diagram I f and schematically illustrates this reduction in the degree of freedom for accumulation.

Such considerations can form the basis for interpreting the peak-to-background contrast ratio in the $I^{(3)}D4WM$ interferogram analyzed in this paper. For the signal at $\mathbf{k}_s = 2\mathbf{k} - \mathbf{k}'$ considered here, the ideas above suggest a very large contrast ratio for samples having long-lived excited states. This is in fact qualitatively the case [3]. For $\tau_c \approx T_2 \ll T_1$, the intensity of the τ -dependent signal is seen to vary as $(T_1/\tau_c)^2$ (the limit of the analytic results for $\tau_c \approx T_2 \ll T_1$) due to the two accumulation degrees of freedom. In contrast, the τ -independent diagram varies as T_1/τ_c from the loss of one accumulation degree of freedom. Thus (for $T_1 \gg T_2$ or τ_c) the peak-to-background contrast ratio varies roughly as T_1/τ_c . For lifetimes that approach either the dephasing time or the coherence time of the light this simple view fails.

VI. OTHER NOISY LIGHT SPECTROSCOPIES

Peak-to-background contrast ratios for various other noisy light spectroscopies can also be explored using the FTC diagrams, in some cases quantitatively. A quick guess as to the contrast ratio of a given spectroscopy can be made by recalling the following: (i) when $\tau=0$ all arrows turn into straight lines and (ii) when $\tau=\infty$ all the contributions to the signal from diagrams that contain arrows must vanish. In the $I^{(3)}$ D4WM spectroscopy considered here, we see that at $\tau=0$ none of the τ -dependent diagrams become identical to the τ -independent diagrams. They remain much less interchromophore synchronized than the triply synchronized background terms. For them additional accumulation is available; thus a large contrast ratio is predicted. This approach is briefly extended to other spectroscopies though without displaying their FTC diagrams. Appropriate FTC diagrams may be easily constructed using the rules presented in Appendix B. They are not shown here.

A. $I^{(2)}$ SHG

In second-harmonic generation (SHG) (a $\chi^{(2)}$ spectroscopy) the beam configuration can be exactly the same as in the above spectroscopy, but now the signal at $\mathbf{k}_s=\mathbf{k}+\mathbf{k}'$ is considered. Stochastic averaging in the treatment of $\chi^{(2)}$ spectroscopies results in four-point correlators rather than six-point correlators. These are similarly broken down using the complex Gaussian moment theorem, each giving four terms that have two pair correlators as factors. Thus the FTC diagrams have only two segments (arrows or lines). $I^{(2)}$ SHG is described by 128 FTC diagrams for fully nonresonant material response. However, there is a 16-fold redundancy; thus there are only eight (four τ -dependent and four τ -independent) distinct diagrams. It is discovered that at $\tau=0$ the τ independent diagrams match one to one with the τ -independent diagrams. Since at $\tau=\infty$ the τ -dependent terms vanish the predicted contrast ratio is (ideally) 2:1. This is in fact the case [4,19].

B. “In-phase” and “out-of-phase” $I^{(2)}$ D4WM

For “in-phase” and “out-of-phase” $I^{(2)}$ D4WM spectroscopies [9,19], in which the third field is from a monochromatic source, the BOX beam configuration [4] is used. (The BOX configuration consists of three parallel beams which form an equilateral triangle on the viewing plane, allowing for all phase-matched third-order signals to have distinct \mathbf{k} vectors.) The “in-phase” version is the detection of the signal with k vector $\mathbf{k}_s=\mathbf{k}+\mathbf{k}'-\mathbf{k}_m$, where \mathbf{k}_m is a monochromatic beam. Here again it is found that the τ -dependent and τ -independent diagrams match one to one at $\tau=0$. Thus a 2:1 contrast ratio is predicted and observed [9,19].

For the “out-of-phase” signal $\mathbf{k}_s=\mathbf{k}-\mathbf{k}'+\mathbf{k}_m$, one observes no reduction at $\tau=0$ of the τ -dependent FTC diagrams to the τ -independent ones. One predicts a large contrast ratio. This is in fact the case [9,19].

C. Three-beam $I^{(3)}$ D4WM

Three-beam $I^{(3)}$ D4WM spectroscopy in which the twice-acting F acts out of phase differs from the presently analyzed

two-beam $I^{(3)}$ D4WM (where F acts twice but in phase) and calls for a three-beam BOX configuration where we consider the signal at $\mathbf{k}_s=\mathbf{k}_a+\mathbf{k}'-\mathbf{k}_b$. \mathbf{k}_a and \mathbf{k}_b are noncollinear beams originating from same field F . In this case it turns out that there are 96 FTC diagrams to consider (triple resonance only). These 96 group into distinct sets—one having only one s -line- t -line synchronization, the other having three synchronizations. The FTC diagrams for the first group match 3:1 (τ -dependent: τ -independent) at $\tau=0$; and the second group matches 1:1. Since the first group of FTC diagrams should strongly dominate the signal (they have only one interchromophore synchronization, not three), we predict a peak-to-background ratio that approaches 4:1 from below. This needs experimental verification.

D. Electronically nonresonant $I^{(2)}$ CRS

Coherent Raman spectroscopies such as CARS and CSRS are dominated by terms having a Raman resonance after the second field intervention. The Diagrams representing the expanded density matrix elements for CARS and CSRS are found elsewhere [20]. Both $I^{(2)}$ CSRS and $I^{(2)}$ CARS formally require 256 FTC diagrams (only Raman resonance is considered). However there is an eightfold formal redundancy. Thus the contrast ratio may be captured by examining only 32 FTC diagrams. Here one finds a one-to-one ratio between τ -dependent and τ -independent diagrams. The former exactly turn into the latter at $\tau=0$. Thus one predicts a 2:1 contrast ratio, exactly as observed [20].

VII. CONCLUSION

We have shown how the use of a simple Bloch two-level system interacting with noisy light having a Lorentzian spectral density may yield much insight into the interesting physics of noisy light spectroscopies. The introduction of the FTC diagrams aids in the analytic calculation as well as in deducing a physical interpretation. It was argued how the added t -line- s -line synchronization of the τ -independent diagrams diminishes their importance relative to the τ -dependent diagrams having event correlator pairs that are free to independently slide (or accumulate strength) over the lifetime decay. The striking asymmetries seen in the τ dependence of the signal were analytically demonstrated and diagrammatically realized. Features include a peak shift from $\tau=0$ and the fact that the excited-state lifetime signal appears only in the decay of the interferogram seen at negative τ . These asymmetries have absolutely nothing to do with inhomogeneous broadening, a spreading of the natural Bohr frequency which is entirely absent in the present model. The complementary interferogram is generated by $\mathbf{k}_s=2\mathbf{k}'-\mathbf{k}$. The interesting issue of the expected contrast ratio was examined where the τ -independent terms were qualitatively taken into account. Finally, the FTC-diagram-based arguments were briefly applied to other noisy light spectroscopies, to confirm and predict their expected peak-to-background contrast ratios.

ACKNOWLEDGMENTS

We express our thanks to Alan Man for his careful reading of the initial draft, to Michael Stimson for his valuable comments which improved the paper, and to Kelly Case for her enthusiastic effort in generating and confirming FTC diagrams for several spectroscopies. We are grateful to the National Science Foundation (Grant No. CHE-9311959) for support of this work.

APPENDIX A

Here we list the triplets of pair correlators that result from the breakdown of the six-point correlators in Eqs. (21)–(24).

I

- a: $\langle p(s_2 - \tau)p^*(s_1) \rangle \langle p(t_1)p^*(t_2 - \tau) \rangle \langle p(t_3)p^*(s_3) \rangle$,
- b: $\langle p(s_2 - \tau)p^*(s_3) \rangle \langle p(t_1)p^*(t_2 - \tau) \rangle \langle p(t_3)p^*(s_1) \rangle$,
- c: $\langle p(s_2 - \tau)p^*(s_1) \rangle \langle p(t_3)p^*(t_2 - \tau) \rangle \langle p(t_1)p^*(s_3) \rangle$,
- d: $\langle p(s_2 - \tau)p^*(s_3) \rangle \langle p(t_3)p^*(t_2 - \tau) \rangle \langle p(t_1)p^*(s_1) \rangle$,
- e: $\langle p(s_2 - \tau)p^*(t_2 - \tau) \rangle \langle p(t_1)p^*(s_3) \rangle \langle p(t_3)p^*(s_1) \rangle$,
- f: $\langle p(s_2 - \tau)p^*(t_2 - \tau) \rangle \langle p(t_1)p^*(s_1) \rangle \langle p(t_3)p^*(s_3) \rangle$.

II

- a: $\langle p(s_2 - \tau)p^*(s_1) \rangle \langle p(t_2)p^*(t_1 - \tau) \rangle \langle p(t_3)p^*(s_3) \rangle$,
- b: $\langle p(s_2 - \tau)p^*(s_3) \rangle \langle p(t_2)p^*(t_1 - \tau) \rangle \langle p(t_3)p^*(s_1) \rangle$,
- c: $\langle p(s_2 - \tau)p^*(s_1) \rangle \langle p(t_3)p^*(t_1 - \tau) \rangle \langle p(t_2)p^*(s_3) \rangle$,
- d: $\langle p(s_2 - \tau)p^*(s_3) \rangle \langle p(t_3)p^*(t_1 - \tau) \rangle \langle p(t_2)p^*(s_1) \rangle$,
- e: $\langle p(s_2 - \tau)p^*(t_1 - \tau) \rangle \langle p(t_2)p^*(s_3) \rangle \langle p(t_3)p^*(s_1) \rangle$,
- f: $\langle p(s_2 - \tau)p^*(t_1 - \tau) \rangle \langle p(t_2)p^*(s_1) \rangle \langle p(t_3)p^*(s_3) \rangle$.

III

- a: $\langle p(s_1 - \tau)p^*(s_2) \rangle \langle p(t_1)p^*(t_2 - \tau) \rangle \langle p(t_3)p^*(s_3) \rangle$,
- b: $\langle p(s_1 - \tau)p^*(s_3) \rangle \langle p(t_1)p^*(t_2 - \tau) \rangle \langle p(t_3)p^*(s_2) \rangle$,
- c: $\langle p(s_1 - \tau)p^*(s_2) \rangle \langle p(t_3)p^*(t_2 - \tau) \rangle \langle p(t_1)p^*(s_3) \rangle$,
- d: $\langle p(s_1 - \tau)p^*(s_3) \rangle \langle p(t_3)p^*(t_2 - \tau) \rangle \langle p(t_1)p^*(s_2) \rangle$,
- e: $\langle p(s_1 - \tau)p^*(t_2 - \tau) \rangle \langle p(t_1)p^*(s_3) \rangle \langle p(t_3)p^*(s_2) \rangle$,
- f: $\langle p(s_1 - \tau)p^*(t_2 - \tau) \rangle \langle p(t_1)p^*(s_2) \rangle \langle p(t_3)p^*(s_3) \rangle$.

IV

- a: $\langle p(s_1 - \tau)p^*(s_2) \rangle \langle p(t_2)p^*(t_1 - \tau) \rangle \langle p(t_3)p^*(s_3) \rangle$,
- b: $\langle p(s_1 - \tau)p^*(s_3) \rangle \langle p(t_2)p^*(t_1 - \tau) \rangle \langle p(t_3)p^*(s_2) \rangle$,
- c: $\langle p(s_1 - \tau)p^*(s_2) \rangle \langle p(t_3)p^*(t_1 - \tau) \rangle \langle p(t_2)p^*(s_3) \rangle$,
- d: $\langle p(s_1 - \tau)p^*(s_3) \rangle \langle p(t_3)p^*(t_1 - \tau) \rangle \langle p(t_2)p^*(s_2) \rangle$,
- e: $\langle p(s_1 - \tau)p^*(t_1 - \tau) \rangle \langle p(t_2)p^*(s_3) \rangle \langle p(t_3)p^*(s_2) \rangle$,
- f: $\langle p(s_1 - \tau)p^*(t_1 - \tau) \rangle \langle p(t_2)p^*(s_2) \rangle \langle p(t_3)p^*(s_3) \rangle$.

Due to stationarity, pair correlators of the form

$$\begin{aligned} \langle p(a - \tau)p^*(b - \tau) \rangle &= \langle p(a - b - \tau + \tau)p^*(0) \rangle \\ &= \langle p(a - b)p^*(0) \rangle \end{aligned}$$

are τ independent.

APPENDIX B

In this Appendix we give the details regarding the construction of the FTC diagrams from the triplet of pair correlators and on how to obtain the analytic contribution from a given diagram. To aid in familiarizing the reader with the FTC diagrams we shall consider diagram I b of Fig. 3 as an example.

1. Rules for constructing a FTC diagram

- (1) Draw two horizontal lines representing the t and s time lines.
- (2) Draw short vertical tick marks on each of the lines to represent the field interventions. Time increases from left to right.
- (3) Draw a straight line (no arrow head) connecting the time events involved in τ -independent pair correlators.
- (4) Draw a curved arrow between time events connected by each τ -dependent pair correlator. The arrow head points to the time at which the τ -containing field (F' for this treatment) intervenes.

2. Rules for obtaining the analytic results (zero detuning)

The point at which an arrow or line connects to a time line is termed a *vertex*, and the arrow or line itself is designated a *segment*.

- (0) All terms contain a factor of $(\pi\Gamma\gamma_{mg}^2)^{-1}$.

The vertex contributions follow.

- (1) Straight-line vertices at t_3 or s_3 give a γ_{mm}^{-1} factor.
- (2) Straight-line vertices at t_1 or s_1 give a γ_{mg}^{-1} factor.
- (3) Arrow head or tail vertices at t_3 or s_3 give a $(\Gamma + \gamma_{mm})^{-1}$ factor.
- (4) Arrow head or tail vertices at t_1 or s_1 give a $(\Gamma + \gamma_{mg})^{-1}$ factor.
- (5) Vertices at t_2 or s_2 make no contribution.

The segment contributions are as follows.

- (6) Straight-line segments make no contribution.
- (7a) For negative τ we have the following.
 - (i) Any arrow pointing to the right gives a $(-e^{\Gamma\tau})$ factor.
 - (ii) Any left-pointing arrow linking t_1 and t_2 or s_1 and s_2 gives a factor

$$\frac{(\Gamma + \gamma_{mg})e^{\Gamma\tau} - 2\Gamma e^{\gamma_{mg}\tau}}{\Gamma - \gamma_{mg}}.$$

- (iii) Any left-pointing arrow linking t_3 and t_2 or s_3 and s_2 gives a factor

$$\frac{(\Gamma + \gamma_{mm})e^{\Gamma\tau} - 2\Gamma e^{\gamma_{mm}\tau}}{\Gamma - \gamma_{mm}}.$$

- (iv) Any left-pointing arrow linking t_1 and t_3 or s_1 and s_3 gives a factor

$$\frac{(\Gamma + \gamma_{mm})(\Gamma + \gamma_{mg})(\gamma_{mm} - \gamma_{mg})e^{\Gamma\tau} - 2\Gamma(\gamma_{mm}^2 - \Gamma^2)e^{\gamma_{mm}\tau} - 2\Gamma(\Gamma^2 - \gamma_{mg}^2)e^{\gamma_{mg}\tau}}{(\Gamma - \gamma_{mm})(\Gamma - \gamma_{mg})(\gamma_{mg} - \gamma_{mm})}.$$

(7b) For positive τ we have the following.

- (i) Any arrow pointing to the left gives a $(-e^{-\Gamma\tau})$ factor.
- (ii) Any right-pointing arrow spanning t_1 and t_2 or s_1 and s_2 gives a factor

$$\frac{(\Gamma + \gamma_{mg})e^{-\Gamma\tau} - 2\Gamma e^{-\gamma_{mg}\tau}}{\Gamma - \gamma_{mg}}.$$

(8) Multiply the factors generated by all segments and vertices to produce the analytic expression for the FTC interferogram at zero detuning.

3. An example

Consider term I b. Here the triplet of pair correlators is

$$\langle p(s_2 - \tau)p^*(s_3) \rangle \langle p(t_1)p^*(t_2 - \tau) \rangle \langle p(t_3)p^*(s_1) \rangle.$$

The first pair correlator produces an arrow segment connecting s_3 and s_2 with its arrow head at s_2 . The second pair correlator produces an arrow segment connecting t_1 and t_2 with its head at t_2 . Finally, the last correlator is τ independent and is thus a straight line connecting t_3 and s_1 . From this FTC diagram we apply the above rules to obtain the

analytic expression for its contribution to the total signal. It is built up as follows: rule (0) $\Rightarrow (\pi\Gamma\gamma_{mg}^2)^{-1}$, rule (1) $\Rightarrow \gamma_{mm}^{-1}$, rule (2) $\Rightarrow \gamma_{mg}^{-1}$, rule (3) $\Rightarrow (\Gamma + \gamma_{mm})^{-1}$, rule (4) $\Rightarrow (\Gamma + \gamma_{mg})^{-1}$, rule (7ai) $\Rightarrow -e^{\Gamma\tau}$,

$$\text{rule (7aiii)} \Rightarrow \frac{(\Gamma + \gamma_{mm})e^{\Gamma\tau} - 2\Gamma e^{\gamma_{mm}\tau}}{\Gamma - \gamma_{mm}},$$

$$\text{rule (7bi)} \Rightarrow -e^{-\Gamma\tau},$$

$$\text{rule (7bii)} \Rightarrow \frac{(\Gamma + \gamma_{mg})e^{-\Gamma\tau} - 2\Gamma e^{-\gamma_{mg}\tau}}{\Gamma - \gamma_{mg}}.$$

The total expression comes from rule (8):

$$\frac{-e^{\Gamma\tau}[(\Gamma + \gamma_{mm})e^{\Gamma\tau} - 2\Gamma e^{\gamma_{mm}\tau}]}{\pi\Gamma\gamma_{mg}^3\gamma_{mm}(\Gamma - \gamma_{nn})(\Gamma + \gamma_{mg})(\Gamma + \gamma_{mm})} \quad (\tau < 0),$$

$$\frac{-e^{-\Gamma\tau}[(\Gamma + \gamma_{mg})e^{-\Gamma\tau} - 2\Gamma e^{\gamma_{mg}\tau}]}{\pi\Gamma\gamma_{mg}^3\gamma_{mm}(\Gamma + \gamma_{mg})(\Gamma + \gamma_{mm})(\Gamma - \gamma_{mg})} \quad (\tau > 0).$$

These two forms are identically recovered from the analytic solution in the limit of zero detuning.

-
- [1] N. Morita and T. Yajima, *Phys. Rev. A* **30**, 2525 (1984).
 - [2] S. Asaka, H. Nakatsuka, M. Fujiwara, and M. Matsuoka, *Phys. Rev. A* **29**, 2286 (1984); R. Beach and S. R. Hartmann, *Phys. Rev. Lett.* **53**, 663 (1984).
 - [3] K. Kurakawa, T. Hattori, and T. Kobayashi, *Phys. Rev. A* **36**, 1298 (1987); A. Debarre, J.-L. Le Gouët, I. Largeré, and P. Techénio, *J. Phys. B* **26**, 3435 (1993); J. Liu, S. Huang, W. Qin, and J. Yu, *J. Lumin.* **54**, 319 (1993); Y. Cui, M. Zhao, G. S. Hue, and P. N. Prasad, *J. Phys. Chem.* **95**, 6842 (1991); R. Beach, D. Debeer, and S. R. Hartmann, *Phys. Rev. A* **32**, 3467 (1985); Y. Zhang, F. Moshary, and S. R. Hartmann, *Laser Phys.* **5**, 676 (1995).
 - [4] M. A. Dugan and A. C. Albrecht, *Phys. Rev. A* **43**, 3877 (1991).
 - [5] M. A. Dugan, J. S. Melinger, and A. C. Albrecht, *Chem. Phys. Lett.* **147**, 411 (1988).
 - [6] A. Lau, A. Kummrow, M. Pfeiffer, and S. Woggon, *J. Raman Spectrosc.* **25**, 607 (1994); K. Wynne, M. Müller, and J. D. W. VanVoorst, *Phys. Rev. A* **41**, 6361 (1990); T. Kobayashi, A. Terasaki, T. Hattori, and K. Kurakawa, *Appl. Phys. B* **47**, 107 (1988); T. Hattori, A. Terasaki, and T. Kobayashi, *Phys. Rev. A* **35**, 715 (1987); A. Kummrow, *Chem. Phys. Lett.* **236**, 362 (1995); A. Kummrow, S. Woggon, and A. Lau, *Phys. Rev. A* **50**, 4264 (1994).
 - [7] P. A. Apanasevich, V. P. Kozich, and A. I. Vodschtiz, *J. Mod. Opt.* **35**, 1933 (1988); H. Nakatsuka *et al.*, *Opt. Commun.* **74**, 219 (1989); K. Misawa, T. Hattori, and T. Kobayashi, *Opt. Lett.* **14**, 453 (1989).
 - [8] S. P. Smith, Ph.D. thesis, Cornell University, 1995.
 - [9] A. C. Albrecht *et al.*, *Laser Phys.* **5**, 667 (1995).
 - [10] K. Wynne and M. Müller, Ph.D. thesis, University of Amsterdam, 1990; T. Kobayashi, *Adv. Chem. Phys.* **85**, 55 (1994).
 - [11] D. Lee and A. C. Albrecht, in *Advances in Infrared and Raman Spectroscopy*, edited by R. J. Clark and R. E. Hester (Wiley-Heyden, New York, 1985), Vol. 12, p. 129.
 - [12] Y. R. Shen, *The Principles of Nonlinear Optics* (Wiley, New York, 1984); P. N. Butcher and D. Cotter, *The Elements of Nonlinear Optics* (Cambridge University Press, New York, 1990).
 - [13] N. Bloembergen, H. Lotem, and R. Lynch, *Indian J. Pure Appl. Chem.* **16**, 151 (1978).
 - [14] J. W. Goodman, *Statistical Optics* (Wiley, New York, 1985).
 - [15] J. T. Manassah and B. Gross, *Laser Phys.* **5**, 490 (1995).
 - [16] D. A. MaQuarrie, *Statistical Mechanics* (Harper Collins, New York, 1976).
 - [17] Wolfram Research, *Mathematica for Windows, Student Edition*, ver. 2.2, 1991.
 - [18] R. Loudon, *The Quantum Theory of Light*, 2nd ed. (Oxford University Press, New York, 1990).
 - [19] D. K.-L. Tan, Ph.D. thesis, Cornell University, 1995.
 - [20] S. A. Schaertel and A. C. Albrecht, *J. Raman Spectrosc.* **25**, 545 (1994); S. A. Schaertel, Ph.D. thesis, Cornell University, 1994.